Discrete element modelling of large soil deformations under heavy vehicles

Viktor Wiberg[a], Martin Servin[a,*], Tomas Nordfjell[b]

[a] *Umeå University, SE-90187, Umeå, Sweden*
[b] *Swedish University of Agricultural Sciences, SE-90183, Umeå, Sweden*

Abstract

This paper addresses the challenges of creating realistic models of soil for simulations of heavy vehicles on weak terrain. We modelled dense soils using the discrete element method with variable parameters for surface friction, normal cohesion, and rolling resistance. To find out what type of soils can be represented, we measured the internal friction and bulk cohesion of over 100 different virtual samples. To test the model, we simulated rut formation from a heavy vehicle with different loads and soil strengths. We conclude that the relevant space of dense frictional and frictional-cohesive soils can be represented and that the model is applicable for simulation of large deformations induced by heavy vehicles on weak terrain.

Keywords: DEM, Multibody Dynamics, Weak Soil, Rut Formation, Multipass

1. Introduction

The discrete element method (DEM) is emerging as a practical and valuable tool for terramechanical studies. Research in this area has focused mostly on vehicle performance and less on the effects on the terrain. Particle-based soil models in DEM simulations can express large plastic deformations, fracture and transition into rapid, irregular flow. The drawback is that DEM simulations are computationally intense. With current technology it is not possible to model large terrains, comparable in size to a full vehicle, with the true distributions of particle size and shape. A common solution is to use *pseudo-particles*, often with spherical shape, and of size chosen as large as possible to reduce their numbers. The pseudo-particle approach is faster to compute, but unable to resolve deformations at length scales smaller than pseudo-particle sizes. On one hand, DEM studies of vehicles and pseudo-particle soil show the ability to simulate important interaction effects, e.g. [1, 2, 3]. On the other hand, subsoil deformations under surface loads may occur in localized shear bands. The width of the shear bands depend on pseudo-particle size, which affects soil bearing capacity [4]. As a consequence, it is not clear that DEM with pseudo-particles can be used to study soil deformations due to wheel-soil interaction from heavy vehicles.

Large plastic deformations occur in the formation of ruts, i.e. the tracks caused by one or more passes of a vehicle with load exceeding the soil bearing capacity. Even at low vehicle speeds, when the soil is in the quasi-static regime, the complex soil behaviour in rut development is challenging to simulate. Rut formation depends on the subsoil stress distribution from an applied load and is a process of repetitive compression and shearing associated with soil compaction and shear displacements. The susceptibility to compaction depends highly on moisture content and initial porosity. At high moisture content, soil shear strength is low and pore pressures resist compaction. Dense soils have a tendency to dilate when sheared which causes volume expansion rather than compaction. In this paper we focus on dense soils with limited or no susceptibility to compaction. These are widespread, and even in the case of contractive soils the main contribution to rut formations is often shear deformations [5]. For dense soils, the cause of material failure due to vehicle interaction is well reflected on the resulting ruts. Thus, the capability to represent rut formation is a strong indication that shear deformations are captured by the model.

The bulk mechanical properties of soil modelled with pseudo-particles depend on particle size, shape, elasticity, friction, restitution, and rolling resistance. A common procedure is to calibrate the particle parameters so that the bulk properties of a specific material measured in a physical test match those of the corresponding virtual test [6]. For example, the internal friction and cohesion of a triaxial test [7, 8], or the cone index measured in a cone penetrometer test [9]. The calibration process is tedious and without standard protocol [6]. Consequently, calibration is usually performed only on a single or a small set of soil samples. Natural soil, however, show large variability in the bulk mechanical properties, both in space and over time. Ability to carry out many simulations on a wide spectrum of soils, with known mechanical properties, is therefore important. At the current stage of DEM-soil modelling with pseudo-particles, it is not clear that each relevant set of soil strength parameters has a matching set

*Corresponding author
Email address: martin.servin@umu.se (Martin Servin)

of pseudo-particle parameters.

The cone index is a composite quantity that depends on the internal friction and bulk cohesion and a common indicator of soil bearing capacity. A strength of the cone index is the relative ease of doing field measurement using a cone penetrometer. Also, the cone index has proved useful for predicting the rut depth from a passing vehicle with given load and wheel properties. These WES-based rut depth models were originally developed for military applications but have also been extended to forestry operations [10]. The rut depth evolution after multiple vehicle passes can empirically be modelled as a function of the first pass rut depth, the number of passes and a *multipass coefficient* [11]. The latter has an established range depending on vehicle load and soil bearing capacity [10, 12, 13].

To answer which soils can be represented using a dense arrangement of spherical pseudo-particles, we created over 100 virtual soil samples with different microscopic model parameters. The bulk-mechanical properties were examined using a triaxial test and quantified in terms of the internal friction and cohesion. For a selection of seven virtual soils, we also characterized the soil strength by simulating the cone penetrometer test. This results in a cone index for each selected soil.

To answer if large shear deformations can be predicted using pseudo-particles, we simulated repeated passes with a heavy vehicle over terrain beds with known cohesion, internal friction, and cone index. The rut depths were compared with empirical models and an experimental data set found in literature [14]. Our comparison with empirical models presents to which extent realistic rut formations can be simulated with respect to cone index, vehicle load, and wheel dimensions. We focus on empirical models since comparisons with physical experiments of a specific soil and vehicle give little insight to how well the simulated measurements generalize to other cases. To make prediction for other cases, experimental data should be gathered from them as well and analysed statistically. This is a lengthy task, already partially performed in the work behind the empirical models.

1.1. Related work

Most examples of using the discrete element method for studying tyre-terrain interaction are limited to two-dimensional analysis or light-weighted vehicles, such as planetary rovers [15, 16]. In [1] it was shown that DEM is significantly better at predicting wheel performance on granular terrain than traditional Bekker-type terramechanics methods, which is fast to compute but limited to steady-state and simplistic wheel geometries. A recent contribution shows the potential in DEM simulations by studying stress transmission under agricultural traffic in comparison with continuum methods [17]. The authors use spherical particles with blocked rotations in a porous soil representation. In a concurrent paper the normal vertical stress was evaluated with field experiments [3]. A study of wheel rutting and mobility of heavy vehicles using particle-based terrain modelling in three dimension is presented in [2]. That paper, by Recuero et al., demonstrates that particle-based terrain in combination with multibody dynamics is indeed a feasible and versatile combination of simulation models for the study of heavy vehicle and terrain interaction. The qualitative behaviour agrees well with established theory of terramechanics. The particle parameters were, however, not calibrated to any specific soil and the bulk-mechanical properties were not examined. The simulated rut formation can therefore not be compared quantitatively with any empirical models and experimental data.

2. Modelling

We assume that vehicles and mechanical devices can be modelled as rigid multibody systems (MBS) and the soil using the discrete element method (DEM). Traditionally, these models are combined using co-simulation. Instead, we used a unified framework based on discrete variational mechanics and nonsmooth dynamics [18, 19]. This choice was motivated by computational speed, numerical stability and avoidance of non-physical coupling parameters that need tuning.

2.1. Discrete mechanics with contacts

The state of a rigid multibody system with N_b bodies, N_j joints and actuators and N_c contacts is represented on descriptor form in terms of the system position, $\boldsymbol{x}(t) \in \mathbb{R}^{6N_\mathrm{b}}$, velocity, $\boldsymbol{v}(t) \in \mathbb{R}^{6N_\mathrm{b}}$, and Lagrange multipliers, $\boldsymbol{\lambda}_\mathrm{j}(t) \in \mathbb{R}^{6N_\mathrm{j}}$ and $\boldsymbol{\lambda}_\mathrm{c}(t) \in \mathbb{R}^{6N_\mathrm{c}}$, that are responsible for the constraint forces due to the joints and contacts. The position variable is a concatenation of the spatial and rotational coordinates of the N_b bodies, $\boldsymbol{x} = [\mathbf{x}, \mathbf{e}]$, and the velocity vector holds the linear and angular velocities, $\boldsymbol{v} = [\mathbf{v}, \boldsymbol{\omega}]$. The time evolution of the multibody system state variables $[\boldsymbol{x}, \boldsymbol{v}, \boldsymbol{\lambda}]$ is given by the following set of equations

$$\boldsymbol{M}\dot{\boldsymbol{v}} = \boldsymbol{f}_\mathrm{ext} + \boldsymbol{G}_\mathrm{j}^\mathrm{T}\boldsymbol{\lambda}_\mathrm{j} + \boldsymbol{G}_\mathrm{c}^\mathrm{T}\boldsymbol{\lambda}_\mathrm{c} \tag{1}$$

$$\varepsilon_\mathrm{j}\boldsymbol{\lambda}_\mathrm{j} + \eta_\mathrm{j}\boldsymbol{g}_\mathrm{j} + \tau_\mathrm{j}\boldsymbol{G}_\mathrm{j}\boldsymbol{v} = \boldsymbol{u}_\mathrm{j}, \tag{2}$$

$$\texttt{contact\_law}(\boldsymbol{v}, \boldsymbol{\lambda}_\mathrm{c}, \boldsymbol{g}_\mathrm{c}, \boldsymbol{G}_\mathrm{c}), \tag{3}$$

where $\boldsymbol{f}_\mathrm{ext}$ is the external force, which like the constraint forces, $\boldsymbol{G}_\mathrm{j}^\mathrm{T}\boldsymbol{\lambda}_\mathrm{j}$ and $\boldsymbol{G}_\mathrm{c}^\mathrm{T}\boldsymbol{\lambda}_\mathrm{c}$, have dimension $\mathbb{R}^{6N_\mathrm{b}}$ and is composed of linear force and torque. The system mass matrix is $\boldsymbol{M} \in \mathbb{R}^{6N_\mathrm{b}\times 6N_\mathrm{b}}$. Eq. (2) is a generic constraint equation. An ideal joint can be represented with $\varepsilon_\mathrm{j} = \tau_\mathrm{j} = \boldsymbol{u}_\mathrm{j} = 0$, in which case Eq. (2) express a holonomic constraint, $\boldsymbol{g}_\mathrm{j}(\boldsymbol{x}) = 0$. A linear or angular motor may be represented by a velocity constraint $\boldsymbol{G}_\mathrm{j}\boldsymbol{v} = \boldsymbol{u}_\mathrm{j}(t)$ with set speed $\boldsymbol{u}_\mathrm{j}(t)$, which follows by $\varepsilon_\mathrm{j} = \eta_\mathrm{j} = 0$ and $\tau_\mathrm{j} = 1$. In the general case, Eq. (2) models a joint with constraint function $\boldsymbol{g}_\mathrm{j}(\boldsymbol{x})$, Jacobian $\boldsymbol{G} = \partial\boldsymbol{g}/\partial\boldsymbol{x}$, joint compliance ε_j and viscous damping rate τ_j. The holonomic and nonholonomic constraints can be seen as the limit of a stiff potential, $\mathcal{U}_\varepsilon = \frac{1}{2\varepsilon}\boldsymbol{g}^T\boldsymbol{g}$, or a Rayleigh dissipation function, $\mathcal{R}_\tau = \frac{1}{2\tau}(\boldsymbol{G}\boldsymbol{v})^T\boldsymbol{G}\boldsymbol{v}$, respectively. This offers the possibility of mapping known models of viscoelasticity to the compliant constraints. Descriptor form means that no coordinate reduction is made. The system is represented explicitly with its full degrees of freedom, although the presence of constraints. This is necessary for allowing non-ideal joints and for dynamic contacts at arbitrary locations.

We use a semi-implicit discrete variational time-stepping algorithm, that is presented in Appendix A together with a description of the equation solver. Here, we simply represent this as a function Φ for advancing the system state at fixed time-step Δt from time t_i to $t_{i+1} = t_i + \Delta t$

$$[\boldsymbol{x}_{i+1}, \boldsymbol{v}_{i+1}, \boldsymbol{\lambda}_{i+1}] = \Phi\left(\boldsymbol{x}_i, \boldsymbol{v}_i, \Delta t, \boldsymbol{g}, \boldsymbol{G}, \boldsymbol{p}\right) \tag{4}$$

where $\boldsymbol{p}$ are the model parameters. The constraint functions and Jacobians are evaluated at every time-step, based on the present configuration of joints and contacts, computed by means of geometric collision detection. We furthermore consider the system to have *nonsmooth dynamics* [20]. That means that the velocity and Lagrange multipliers are allowed to be arbitrarily discontinuous to reflect instantaneous changes due to impacts, frictional stick-slip transitions or joints and actuators reaching set limits. This is unavoidable when using an implicit integration scheme because of the coupling between state variables trough the contact law Eq. (3). Normal contacts and Coulomb friction is introduced as simple inequality constraints and complementarity conditions.

The contact law between particles include models for cohesive viscoelastic normal contacts (n), tangential Coulomb friction (t), and rolling resistance (r). These are formulated in terms of inequality and complementarity conditions. The resulting model can be seen as a time-implicit version of the conventional discrete element method (DEM) and is therefore referred to as nonsmooth DEM (NDEM) [21, 19]. We use the following conditions as `contact_law` for each contact:

$$0 \leq \varepsilon_\mathrm{n}\lambda_\mathrm{n} + g_\mathrm{n} + \tau_\mathrm{n}\boldsymbol{G}_\mathrm{n}\boldsymbol{v} \perp (\lambda_\mathrm{n} + \bar{\lambda}_\mathrm{c}) \geq 0 \tag{5}$$

$$\gamma_\mathrm{t}\boldsymbol{\lambda}_\mathrm{t} + \boldsymbol{G}_\mathrm{t}\boldsymbol{v} = 0, \quad |\boldsymbol{\lambda}_\mathrm{t}| \leq \mu_\mathrm{t}|\boldsymbol{G}_\mathrm{n}^\mathrm{T}\lambda_\mathrm{n}| \tag{6}$$

$$\gamma_\mathrm{r}\boldsymbol{\lambda}_\mathrm{r} + \boldsymbol{G}_\mathrm{r}\boldsymbol{v} = 0, \quad |\boldsymbol{\lambda}_\mathrm{r}| \leq r\mu_\mathrm{r}|\boldsymbol{G}_\mathrm{n}^\mathrm{T}\lambda_\mathrm{n}|, \tag{7}$$

where g_n is a function of the contact overlap and the Jacobians, $\boldsymbol{G}_\mathrm{n}$, $\boldsymbol{G}_\mathrm{t}$ and $\boldsymbol{G}_\mathrm{r}$ govern the normal, tangent, and rotational directions of the contact forces. The parameters ε_n, τ_n, γ_t in Eq. (5) control the contact compliance and damping, and $\bar{\lambda}_\mathrm{c} = c_\mathrm{p}A_\mathrm{p}/|\boldsymbol{G}_\mathrm{n}^\mathrm{T}|$ the cohesion, see Appendix A for details. Setting these parameters to zero means that no penetration should occur between elements, $g_\mathrm{n}(\boldsymbol{x}) \geq 0$, and the normal force should be repulsive, $\lambda_\mathrm{n} \geq 0$. The symbol $\perp$ is short notation for that complementarity condition [22]. The inclusion of $\bar{\lambda}_\mathrm{c}$ enables cohesive normal force with maximum value $f_\mathrm{c}^\mathrm{max} = c_\mathrm{p}A_\mathrm{p}$, where c_p is the particle cohesion and A_p is the particle cross section area. The cohesion is active when the contact overlap is smaller than a certain cohesive overlap, that we chose $\delta_\mathrm{c} = 0.025d$. This reduces the effective size of the particles correspondingly. Eq. (6) states that contacts should have zero slide velocity, $\boldsymbol{G}_\mathrm{t}\boldsymbol{v} = 0$, giving rise to a friction force bounded by the Coulomb friction law with friction coefficient μ_t. Similarly, Eq. (7) states that, as long as the constraint torque is no greater than the rolling resistance law, relative rotational motion of contacting bodies is constrained, $\boldsymbol{G}_\mathrm{r}\boldsymbol{v} = 0$. Here, μ_r is the rolling resistance coefficient and r is the particle radius. Each contact adds $\dim(\lambda_\mathrm{n}, \boldsymbol{\lambda}_\mathrm{t}, \boldsymbol{\lambda}_\mathrm{r}) = 6$ additional variables and equations to the system.

We map the normal contact law, Eq. (5), to the nonlinear Hertz-Mindlin contact model, which follows from the theory of linear elasticity [23]. The Hertz-Mindlin normal force is split into an elastic spring force and a viscous damping force

$$\boldsymbol{f}_\mathrm{n} = k_\mathrm{n}\delta^{3/2}\boldsymbol{n} + k_\mathrm{n}c_\mathrm{d}\delta^{1/2}\dot{\delta}\boldsymbol{n}, \tag{8}$$

where $\delta(\boldsymbol{x})$ and $\dot{\delta}(\boldsymbol{x})$ is the contact overlap and penetration velocity of two contacting spherical particles. The spring stiffness coefficient is $k_\mathrm{n} = \frac{1}{3}E^*\sqrt{d^*}$, where $E^* = [(1-\nu_a^2)/E_a + (1-\nu_b^2)/E_b]^{-1}$ is the effective Young's modulus and $d^* = (d_a^{-1} + d_b^{-1})^{-1}$ is the effective diameter for two contacting spheres, a and b, with Young's modulus E_a, diameter d_a and Poisson's ratio ν_a etc. The damping coefficient is c_d. The mapping to Eq. (5) is accomplished by $g_\mathrm{n} = \delta^{5/4}$, $\varepsilon_\mathrm{n} = 5/4k_\mathrm{n}$ and $\tau_\mathrm{n} = \max(5c_\mathrm{d}/4, 4.5\Delta t)$, where the clamping of the damping time is explained in Appendix A.

The particle shape is an important material parameter for granular matter and soil. It is, however, also associated with increased computational complexity in simulations. Both the number of contacts and the time for computing each contact point increases with more complex shapes. It has been shown, both theoretically and experimentally, that many effects of particle angularity can be modelled with spherical particles and rolling resistance [24].

2.2. Soil simulants

Using discrete elements, a virtual analogue of real soil was represented as a packed collection of spherical particles defined as a *soil simulant*. To assure that experiments were conducted with identical packing we used three *simulant templates*, one for the triaxial, cone pentrometer, and rut depth tests. The templates had different dimensions but were prepared in the same way. Initially, particles were emitted inside a closed container with frictionless smooth rigid walls. We used a fixed particle size distribution of $d \in \{24, 34, 40\}$ mm, set to make up 20, 30, and 50 per cent by mass. To achieve a spatially uniform distribution the samples were compressed isotropically at zero particle cohesion c_p, friction μ_t, and rolling resistance μ_r. We found that a pressure of 10 kPa produced dense samples with porosity $\varphi = 0.30$, or packing density of 0.70. Our polydisperse samples are comparable to close-packed equal spheres with packing density $\simeq 0.74$ and therefore limited in compactability. At static equilibrium the state of the soils was saved, as a template, for later use.

During tests, we started with a simulant template and set the model parameters μ_t, μ_r, and c_p to create different soil simulants. Although the simulants did not explicitly contain water, the effects of pore pressures and fluid flow can be viewed as contained in the model parameters[1]. Apart from μ_t, μ_r, and c_p, model parameters were held fixed. Since our study was restricted to the quasistatic regime, the coefficient of restitution, $e = 0$, and particle mass density, $\rho_\mathrm{p} = 2000$ kg/m^3, were assumed to have insignificant effects. Because the particles were moderately stiff, $E_\mathrm{p} = 100$ MPa, $\nu_\mathrm{p} = 0.3$, the bulk elasticity of soil depended more on porosity and particle shape (or effective rolling resistance).

In Appendix B we demonstrate that the simulations are invariant of particle size.

3. Bulk properties of terrain simulants

To assess what type of material a simulant represents, we used bulk mechanical parameters cohesion c and internal friction ϕ, which are standard soil properties in terramechanic studies. These parameter are used to describe soil failure in the Mohr-Coulomb criterion $\tau_\mathrm{f} = c + \sigma_\mathrm{n} \tan\ \phi$. It states that the shear stress at failure τ_f is a function of the normal stress σ_n acting on the failure plane.

Another measure of soil strength is the cone index (CI). The CI is a widely used indicator of soil bearing capacity with original purpose to provide mobility and trafficability assessment for military vehicles [25]. To determine the CI, a cone is pushed into the soil at constant rate while measuring penetration resistance, i.e. the resisting force per cone base area. The penetration resistance is averaged between two depths to get a single value called the CI. The CI has been used to develop empirical models related to rut formations [10].

To determine the CI, c, and ϕ of soil simulants, we simulated two separate bulk tests: the in-situ cone penetrometer test [26] and a consolidated drained triaxial test [27].

3.1. The triaxial cell

The triaxial cell was modelled as box-shaped (Figure 1) with perfectly smooth rigid wall boundaries. The test was carried out under gravity free conditions and divided into two phases: the consolidation phase and the shear phase. During consolidation the sample was subject to the confining stress level $\sigma_1 = \sigma_2 = \sigma_3$, controlled by monitoring boundary forces and effective areas of each side. The consolidation phase took place until the pressure on each boundary was approximately static. In the shear phase, the vertical walls were driven inward in a strain-controlled manner at 0.25 m/s, corresponding to an inertial number of $I \lesssim 0.0025$ in the quasistatic regime [28]. The major stress σ_1 was registered over time as the lateral walls were adjusted to maintain constant minor stresses until the axial strain reached 25%.

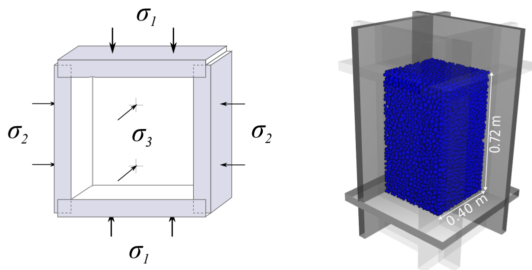

Figure 1: Illustration of the triaxial cell with plane side-walls (left) and a snapshot image of the simuation model (right).

To evaluate c and ϕ we fitted the Mohr-Coulomb failure criterion to the Mohr-circles drawn from $\sigma_2 = \sigma_3$ and peak strength. The peak strength was taken from simulation data as the largest deviator stress $\sigma_\mathrm{dev} = \sigma_1 - \sigma_3$.

3.2. The cone penetrometer

The cone penetrometer was modelled as a kinematic body consisting of two geometries, the sleeve cylinder and the cone, as shown in Figure 2. The cone had an apex angle of 30° in agreement with the original WES-cone and ASABE standard [26]. Its diameter was chosen to be three times the mean particle diameter [29]. Particle-cone Young's modulus was set to 100 MPa, while μ_t and μ_r were assigned the inter-particle value and particle-cone cohesion and restitution, were set to zero.

After loading the *soil simulant template* and setting model parameters, the top boundary was removed and gravity introduced. It was verified that this action did not noticeably affect the soil porosity or configuration. The width of the template was chosen so that an increase in base sides showed insignificant effects on the resulting penetration resistance.

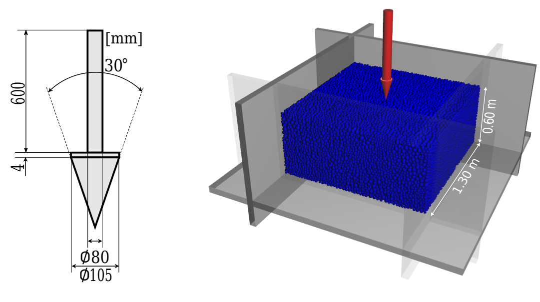

Figure 2: Cone penetrometer illustration (left) and corresponding simulation model (right).

During testing, the penetrometer was driven into the soil with a rate of 0.1 m/s [30], which for numerical convenience is higher than the ASABE standard. However, the inertial

[1] An increase in water content typically lowers the inter-particle tangential friction while increasing the cohesion.

number $I = 0.015$ ensures simulations near the quasistatic regime [28]. The penetration resistance was sampled until the cone tip reached a depth of 0.5 m. To find the CI, the limiting penetration resistance was estimated by the average resistance between 0.4-0.5 m. At larger depth the effect of the bottom boundary becomes dominant.

3.3. Simulations

To investigate the space of numerical soils, we considered 100 combinations of model parameters in the range $c_\mathrm{p} \in [0, 50]$ kPa, $\mu_\mathrm{r} \in [0, 0.2]$, $\mu_\mathrm{t} \in [0, 0.7]$ generated using latin hypercube sampling with uniform distribution. Note that we delimited our paramter search to dense soils with fixed initial porosity. For each sample we determined the stress parameters ϕ and c under $\sigma_2 = \sigma_3 \in \{30, 50\}$ kPa using the triaxial test.

To study the results of the triaxial test in further detail, we extended the original 100 samples with seven manually selected soils. Our intention was to also examine soil space extremities, validate use of the Mohr-Coulomb failure criterion, and find soils to be used in rut depth simulations. Two of the soils were assigned zero inter-particle cohesion c_p, expected to be purely frictional, four were of different cohesive-frictional character and one was expected to be purely cohesive with zero μ_t and μ_r. To check if these soils obeyed the Mohr-Coulomb failure criterion, we included a supplementary confinement pressure of 100 kPa and plotted the three Mohr-circles together with the estimated linear envelope.

Finally, to see how the shear strength parameters were related to CI, we simulated the cone penetrometer test for each of the seven soils. In addition, we need the CI to compare simulated with predicted rut depths.

3.4. Results and discussion

The data of ϕ and c indicated that frictional and cohesive-frictional soils can be represented, while cohesive soils could not, as presented in Figure 3. Despite a dense particle assembly with fixed initial porosity we can simulate soils with $\phi \in [0, 60]^\circ$ and $c \in [0, 30]$ kPa. A soil with high cohesion was only obtained with high inter-particle friction μ_t, leading to an increase in ϕ and resulting in a cohesive-frictional soil. As evident from Figure 3, μ_t was positively correlated with ϕ and c_p with c. However, the rolling resistance coefficient μ_r presented seemingly random behaviour. This phenomenon is explained by the saturation effect of the Coulomb friction law. When an individual contact is in sliding mode, an increase in rolling resistance does not affect the internal friction ϕ. The saturation effect and its influence on the bulk mechanical properties have been thoroughly studied in [31, 32].

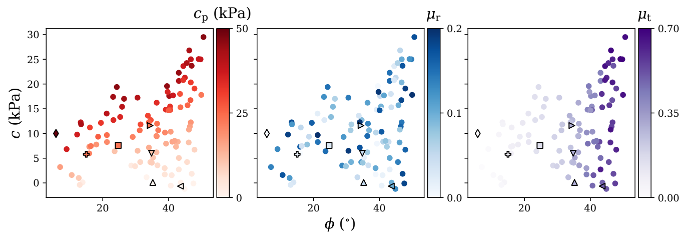

Figure 3: Soil strength parameter space (c, ϕ) using three difference colour maps, one for each model parameter $(c_\mathrm{p}, \mu_\mathrm{r}, \mu_\mathrm{t})$. Deviant markers refer to the complementary seven soils not part of the initial set of 100 samples, see Table 1.

The data from the seven complementary soils showed a variety in soil strength with a positive correlation between CI and the shear strength parameters, summarized in Table 1. As expected, two soils were frictional with near zero cohesion and four cohesive-frictional with non-zero cohesion and internal friction. However, the simulant expected to be cohesive, with no inter-particle friction and rolling resistance, resulted in an above zero internal friction (5.8 °) and only moderate cohesion (10 kPa). For a comparison with the original 100 soils, see the deviant markers in Figure 3.

Table 1: Pseudo-particle parameters and corresponding bulk mechanical properties of the seven complementary soils. Markers in the left most column refer to Figure 3.

	Name	μ_t	μ_r	c_p (kPa)	ϕ (°)	c (kPa)	CI (kPa)
$<$	`fs_strong`	0.50	0.10	0.0	43.6	-0.65	950 ± 77
$\wedge$	`fs_weak`	0.30	0.05	0.0	35.2	0.10	400 ± 44
$>$	`cfs_strong`	0.30	0.05	23.4	34.4	11.6	1080 ± 105
$\vee$	`cfs_medium`*	0.30	0.05	11.7	34.8	6.00	850 ± 51
$\square$	`cfs_weak`*	0.15	0.025	23.4	24.7	7.59	390 ± 21
$+$	`cfs_weakest`	0.06	0.01	23.4	15.0	5.80	160 ± 11
$\lozenge$	`cs_weak`	0.00	0.00	50.0	5.8	10.0	120 ± 8

Soils marked with * were used in rut depth simulations.

The stress-strain curves showed typical characteristics expected from real frictional and cohesive-frictional soils and the Mohr-circles drawn from the peak strengths formed linear envelopes. Figures 4 and 5 show stress-strain curves and Mohr-circles for three simulants: one frictional, one cohesive-frictional, and the soil which was expected to be cohesive. Dense frictional soils tend to have a distinct peak strength followed by a decrease in stress while the decrease in cohesive-frictional soils is less pronounced. This behaviour of real soils was observed for our soil simulants. In contrast, normally consolidated cohesive soils typically attain constant stress after failure and gain no strength with increasing confinement pressure. Therefore, we expected the curves in the upper right panel in Figure 4 to overlap, leading to Mohr-circles with identical radius in the right panel of Figure 5. However, this is not the case and in line with our previous findings, that the particle-based approach is not capable of representing purely cohesive soils. We believe that the stress fluctuations from `cs_weak` (cf. upper right panel of Figure 4) are due to breakage of cohesive bonds, which causes rapid particle displacements. Although the fluctuations affect the peak strength, reducing them by using smaller particles would not result in equal radii Mohr-circles and a purely cohesive soil.

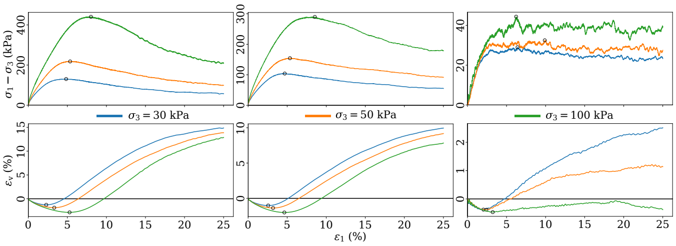

Figure 4: Deviator stress and volumetric strain as a function of axial strain for the soil simulants `fs_strong` (left), `cfs_medium` (middle) and `cs_weak` (right). The markers indicate the peak strength for each of the three confining pressures.

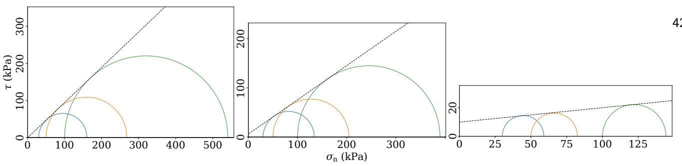

Figure 5: Mohr circles and the resulting Mohr-Coulomb failure envelope from the soil simulants `fs_strong` (left), `cfs_medium` (middle) and `cs_weak` (right).

The results of the cone penetrometer test showed that varying weakness was represented by both frictional and cohesive-frictional soils, see Figure 6. In forest operations, the soils `cfs_strong`, `fs_strong` and `cfs_medium` can be classified as having high ground bearing capacity (CI > 500 kPa), `cfs_weak`, `fs_weak` as medium (CI 300-500 kPa) and `cfs_weakest`, `cf_weak` (CI < 300) as low [33].

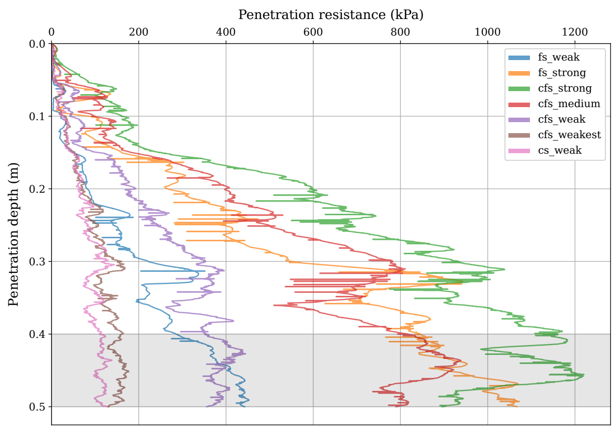

Figure 6: Curves from the cone penetrometer test for seven different numerical soils. The CI is taken as the average penetration resistance between 0.4 and 0.5 m depth (shaded region).

4. Rut depths

In this scenario, terrain simulants were exposed to a heavy vehicle where the resulting rut depth was measured after each one-lane pass. We validated the particle-based terrain models by comparing simulated rut depths with field experiments and empirical models: WES-based and multipass rut depth models.

4.1. WES-based rut depth models

To make rut depth predictions after the first vehicle pass we used the Waterways Experiment Station based rut depth models [10]. The models rely on the CI as a measure of soil strength and combine it with tyre dimensions and wheel load into a empirical quantity called the *wheel numeric*. We used a numeric for tyres operating in cohesive-frictional soils

$$N_{\mathrm{cs}} = \frac{\mathrm{CI}\, b_{\mathrm{ty}}\, d_{\mathrm{ty}}}{W}, \tag{9}$$

where b_{ty} is the tyre width, d_{ty} is the diameter and W is the static wheel load [34].

The N_{cs} numeric has been used as input in different WES-based rut depth models developed for various operating conditions. We considered two models by Anttila from data collected on moraine with peaty depressions. Rut depths were measured after each pass, alternating between an empty and loaded forwarder along the same track but travelling in opposite directions [35].

$$z_{\mathrm{rut}}^{\mathrm{A}_1} = 0.005 + \frac{1.212}{N_{\mathrm{cs}}} \tag{10}$$

$$z_{\mathrm{rut}}^{\mathrm{A}_2} = \left(0.003 + \frac{0.910}{N_{\mathrm{cs}}}\right) d_{\mathrm{ty}}. \tag{11}$$

We also used a model by Saarilahti based on measurements carried out on a single track post vehicle pass on peatlands [36],

$$z_{\mathrm{rut}}^{\mathrm{S}} = \frac{0.432}{N_{\mathrm{cs}}^{0.79}} d_{\mathrm{ty}}. \tag{12}$$

The rut depth models (10)-(12) should not normally be extrapolated to other conditions than those in which they were derived. However, independent studies have shown that these models may provide sufficient rut depth estimations [12]. Therefore, we consider it meaningful to compare empirically based predicted rut depths with simulated ones.

4.2. Multipass rut depth

To compare rut depth evolutions, we relied on the multipass sinkage model [11]

$$\ln z_n = \ln z_1 + \frac{1}{a} \ln n, \tag{13}$$

which has also been successfully applied to rut depths. In such cases z_1 is the rut depth after the first wheel pass,

$n \in \{2, 3, 4, \ldots\}$ is any wheel pass and a is the multipass coefficient. The multipass coefficient can be determined by fitting rut depth data to model (13) using linear regression and typically lies between 2-3 for weak soil. Model (13) has also been used for full vehicles with rut depth measures after three or four wheels, depending on the vehicle, where observed values of a fall in the same range [12].

4.3. Quarter vehicle with two-wheeled bogie

The 3D vehicle model consisted of two main parts, the chassis and the two-wheeled bogie, constrained to move according to the illustrations in Figure 7. The purpose of the chassis was to mimic one quarter of the weight of a full eight-wheeled vehicle and could be adjusted depending on the load case. To obtain forward motion both wheels were driven at fixed angular velocity. Each wheel had Trelleborg 800/65 R32 tractor tyres rescaled to diameter $d = 1.5$ m, width $b = 0.65$ m, and 46 mm tread depth. The tyres were treated as rigid, which is a reasonable model for pneumatic tyres with high inflation pressure on weak soil [25].

To maintain rigid contacts between tyre and particles we used a high contact Young's Modulus of 100 GPa. Tyre-particle cohesion and restitution was set to zero. The sensitivity of rolling resistance and friction coefficient is limited due to the lugs in tread pattern and was set arbitrarily to the inter-particle value and $\mu_{\mathrm{t}} = 0.6$, respectively.

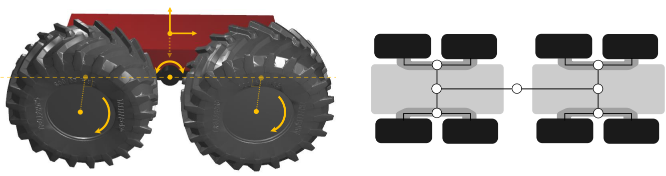

Figure 7: The 3D model of the quarter vehicle (left) and an illustration of a full vehicle (right). The arrows indicate unconstrained directions of motions.

4.4. Rut depth measurements

The vehicle was driven repeatedly over a flat elongated terrain of length 6.5 m, width 1.3 m, and depth 0.6 m, consisting of about 200 000 particles, see Figure 8. The terrain length of 6.5 m allows for ~ 1.4 wheel revolutions and a center patch unaffected by vehicle entry and exit. To achieve steady state travel speed the vehicle was accelerated along an entry strip to its target velocity of 0.5 m/s before entering the terrain at the same level. The vehicle then traversed the terrain to the point where the rear wheel reached an exit strip, at which the simulation state was saved and used as starting point for the next pass. After each pass, the height of the entry and exit strips were adjusted to the rut and the already accelerated vehicle was placed at the entry strip. This procedure was repeated for 10 passes or until the rut exceeded a depth of 15 cm. A sample video is included as supplementary material and also available at `https://youtu.be/20jUWaTSo8A`.

The rut depths were computed at intervals of 0.04 m along a center patch of equal length as the quarter vehicle (3.22 m). In doing so, we avoided the areas closest to the entry and exit strips. Each sectional rut depth was evaluated as the maximum depth relative to the undisturbed surface. The rut depth from a single pass was taken as the average over the sectional depths.

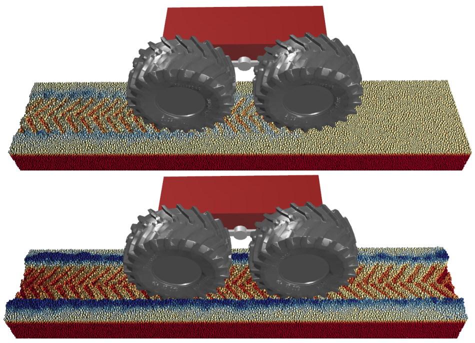

Figure 8: Sample images from a quarter vehicle-terrain simulation during the first (top) and third (bottom) pass. Particles have been colour coded by height, where the difference between deep blue and full red is 0.2 m. The entry and exit strips have been made transparent.

4.5. Simulations

We used the soil simulants `cfs_weak` and `cfs_medium` from Table 1 because rut formations typically occur in cohesive-frictional soils. In addition, their CI indicates leading to distinct rut formations from vehicles with mass comparable to a forwarder.

To study the effect of different load cases on rut depth, three sets of simulations were conducted on the soil type `cfs_weak` using a quarter vehicle mass of 3600, 4400 and 5200 kg. Our intention was to run ten subsequent passes for all load cases. However, due to the deep ruts caused by the heaviest vehicle, boundary effects became concerning and it was decided that only six passes be simulated. We also wanted to compare the rut depths between two soils of different bearing capacity (CI). Therefore, the stronger soil `cfs_medium` was tested by simulating ten passes with the 4400 kg quarter vehicle.

For all four simulation sets, we calculated the predicted rut depths after the first *full* vehicle pass from models (10)-(12). To find out if the multipass coefficient was in the expected range, we used linear regression to fit model (13) to the simulated rut depth evolutions.

4.6. Experimental data

Instead of conducting new experiments we compared simulated rut depths on `cfs_medium` with a data set found in literature [14]. The experimental site was located on a stand of Norway spruce with dry to moist sandy silty till soil. The first pass was taken by a 19700 kg six-wheeled harvester (Timberjack 1270D) with 700 mm wide tyres of 1374 mm diameter on the rear single axle and 1633 mm on the front bogie axles. Pass two to five was driven by an eight-wheeled forwarder (Timberjack 1710B) with four bogies, each equipped with tyres of 750 mm width and 1450 mm diameter. On each plot the forwarder had different tyre pressures of 300, 450, and 600 kPa. Rut depths were measured after the first, second and fifth pass at one point per track. Cone resistance was measured at six points per plot using an Eijkelkamp penetrologger with 30° apex angle and 3.22 cm^2 base area. Both cone resistance and rut depths were taken as the mean per plot over three sections in the stand. Average cone index between 0.11-0.20 m was similar in all three plots and reported as $\sim$ 1200 kPa before the harvester pass. The results showed no significant effect on rut depth from forwarder tyre pressure, motivating our comparison despite using a model with rigid tyres.

We compared rut depth after the harvester pass based on the wheel numeric (9), which encapsulates tyre dimensions, wheel load, and soil strength into a scalar value. Assuming the harvester had even weight distribution, the wheel numerics of the rear and front wheels were N_{cs} = 41.8 and N_{cs} = 35.2, respectively. In the simulation on `cfs_medium` with the 4400 kg vehicle model N_{cs} = 38.3. With similar wheel numerics we expect similar simulated and physical rut depths. To compare multipass effects is more difficult considering the experimental data used different vehicles on the first and second to fifth passes.

4.7. Results

In all four cases, the simulated rut depths after the first vehicle pass were in good agreement with those of the empirical rut depth models (10)-(12) (Figure 9). Rut depth increased linearly with load, which is consistent with models (10) and (11). We also observed that a soil with higher CI led to a shallower rut.

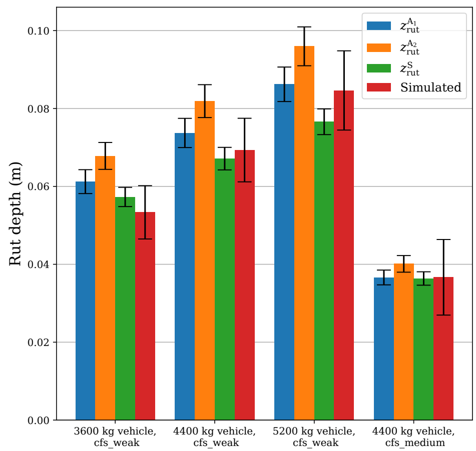

Figure 9: The predicted (blue, orange, green) and simulated (red) rut depths after the first vehicle pass, i.e. the second quarter vehicle. First three left groups are from different vehicle masses on the soil `cfs_weak` and the fourth group from `cfs_medium` and a vehicle mass of 4400 kg. Error bars correspond to one standard deviation.

The simulated rut depth evolutions showed largest effect due to the first pass and a decrease in depth change with number of passes, see Figure 10. Our results showed that a stronger soil was less sensitive to repeated passes and soils became more sensitive when increasing the vehicle load. The curves fitted to the data resulted in multipass coefficients within the expected range. In the case of the heaviest vehicle on `cfs_weak` it was below 2, which is reasonable considering the high load and soil weakness. The other cases resulted in multipass coefficients between 2 and 3, which is consistent with empirical findings for weak soil.

The rut depth in the numerical soil `cfs_medium` was compared to experimental data [14], see Figure 10. Rut depths after the harvester pass was the same on all three experimental plots and agrees well with the simulated measurement. Our results show that physical and simulated rut depths with similar wheel numerics produce similar rut depths.

Consistent with our simulations, the general trend in the experimental data is that the first pass has the greatest impact and subsequent passes cause less change in rut depth. Variability in experimental data is observed as intersecting lines and that the forwarder with lowest tyre pressure (C, 300 kPa) caused the second deepest rut. The fact that the simulated rut depth lies between the experimental curves indicate a good generalization.

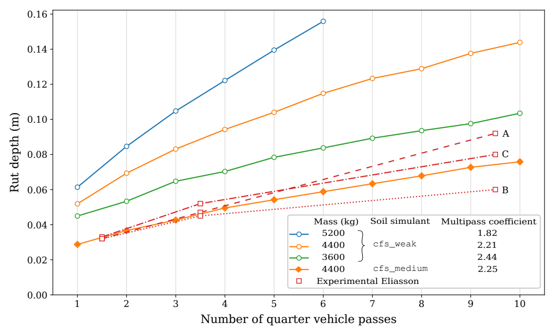

Figure 10: Rut depth evolutions on the soils `cfs_weak` and `cfs_medium`. Only six passes were simulated using the heaviest mass due to the rut exceeding 15 cm. Physical data [14] corresponds to three experimental plots with first pass from a six-wheeled harvester followed by four passes of an eight-wheel forwarder with tyre pressure of 600 (A), 450 (B), and 300 (C) kPa. Note that the harvester with three wheels on each side corresponds to 1.5 quarter vehicle passes.

5. Conclusion

We conclude that large deformations in weak terrain from heavy vehicles can be studied numerically using the discrete element method with a pseudo-particle approach. The relation between rut depth and the terrain's cone index, vehicle weight and tyre dimensions agree well with empirical observations. The terrain models are also capable of capturing the effect from repeated one-lane vehicle passes. Since the soil beds are dense the deformations are primarily due to shear failure and not to compaction.

We characterize dense numerical soils in terms of cohesion and internal friction and show that frictional and cohesive-frictional soils of varying strength can be represented. To model purely cohesive soils, a possible solution is to extend or modify the inter-particle contact model, e.g.

to use parallel bonds [37] or tangential cohesion [38]. The inability to represent purely cohesive soils does not lead to any significant limitations since the majority of trafficable soils are of cohesive-frictional character.

The present approach can enhance the development of vehicles with lesser environmental impact by running simulations on soils with different strength. In future research, the mapping of microscopic model parameters to macroscopic bulk-mechanical properties should be extended to include also porosity and dilatancy angle. Another interesting continuation is the study of soil compaction and stress distribution under controlled and repeatable conditions in a way not possible during field experiments.

6. Acknowledgements

This work has in part been supported by Mistra Digital Forest (Grant DIA 2017/14 #6) and Skogtekniska Klustret AB and Algoryx Simulation AB. The simulations were performed on resources provided by the Swedish National Infrastructure for Computing (SNIC dnr 2019/3-168) at High Performance Computing Center North (HPC2N).

Appendix A. Numerical method

This appendix explains the numerical method for simulating the particle and multibody system.

The equations of motion (1) and (2) form a set of differential algebraic equations (DAE) for the system variables $[\boldsymbol{x}, \boldsymbol{v}, \boldsymbol{\lambda}]$. DAEs are prone to numerical instability for many integration schemes. The theory of discrete variational mechanics offers a way to construct time-stepping algorithms with symmetry-preserving properties for mechanical systems, i.e., preservation of energy and momentum. This, so called, symplectic property of variational integrators guarantee numerical stability and produce numerical solutions that shadow the exact trajectory, although the local error may be larger than with some standard integrators like Runge-Kutta that may diverge with time. SPOOK is a first order accurate discrete variational integrator [39], developed particularly for fixed time-step realtime simulation with non-ideal constraints like Eq. (1)-(2) and for contact laws like Eq. (5)-(7).

The SPOOK stepper is derived from a discrete variational formulation of nonholonomic and non-ideal constraints and has been proven linearly stable [39]. The numerical time integration scheme, $(\boldsymbol{x}_i, \boldsymbol{v}_i) \rightarrow (\boldsymbol{x}_{i+1}, \boldsymbol{v}_{i+1}, \boldsymbol{\lambda}_{i+1})$, for computing the position, velocity, and Lagrange multiplier at time $t_{n+1} = t_n + \Delta t$ from previous state at time t_i involve solving the following mixed complementarity problem (MCP) [22]

$$
\begin{gathered}
\boldsymbol{H}\boldsymbol{z} + \mathbf{b} = \mathbf{w}_l - \mathbf{w}_u \\
0 \leq \mathbf{z} - \mathbf{l} \perp \mathbf{w}_l \geq 0 \\
0 \leq \mathbf{u} - \mathbf{z} \perp \mathbf{w}_u \geq 0
\end{gathered}
\tag{A.1}
$$

where

$$
\boldsymbol{H} = \begin{bmatrix}
\boldsymbol{M} & -\boldsymbol{G}_{\mathrm{n}}^{\mathrm{T}} & -\boldsymbol{G}_{\mathrm{t}}^{\mathrm{T}} & -\boldsymbol{G}_{\mathrm{r}}^{\mathrm{T}} & -\boldsymbol{G}_{\mathrm{j}}^{\mathrm{T}} \\
\boldsymbol{G}_{\mathrm{n}} & \boldsymbol{\Sigma}_{\mathrm{n}} & 0 & 0 & 0 \\
\boldsymbol{G}_{\mathrm{t}} & 0 & \boldsymbol{\Sigma}_{\mathrm{t}} & 0 & 0 \\
\boldsymbol{G}_{\mathrm{j}} & 0 & 0 & \boldsymbol{\Sigma}_{\mathrm{r}} & 0 \\
\boldsymbol{G}_{\mathrm{j}} & 0 & 0 & 0 & \boldsymbol{\Sigma}_{\mathrm{j}}
\end{bmatrix},
\tag{A.2}
$$

$$
\boldsymbol{z} = \begin{bmatrix}
\boldsymbol{v}_{n+1} \\
\boldsymbol{\lambda}_{\mathrm{n},n+1} \\
\boldsymbol{\lambda}_{\mathrm{t},n+1} \\
\boldsymbol{\lambda}_{\mathrm{r},n+1} \\
\boldsymbol{\lambda}_{\mathrm{j},n+1}
\end{bmatrix}, \quad
\boldsymbol{b} = \begin{bmatrix}
-\boldsymbol{M}\boldsymbol{v}_n - \Delta t \boldsymbol{M}^{-1}\boldsymbol{f}_{\mathrm{ext}} \\
\frac{4}{\Delta t}\boldsymbol{\Upsilon}_{\mathrm{n}}\boldsymbol{g}_{\mathrm{n}} - \boldsymbol{\Upsilon}_{\mathrm{n}}\boldsymbol{G}_{\mathrm{n}}\boldsymbol{v}_n \\
0 \\
0 \\
-\boldsymbol{\omega}_{\mathrm{j}} + \frac{4}{\Delta t}\boldsymbol{\Upsilon}_{\mathrm{j}}\boldsymbol{g}_{\mathrm{j}} - \boldsymbol{\Upsilon}_{\mathrm{j}}\boldsymbol{G}_{\mathrm{j}}\boldsymbol{v}_n
\end{bmatrix}.
\tag{A.3}
$$

The solution vector $\boldsymbol{z}$ contains the new velocities and the Lagrange multipliers. The position update is simply $\boldsymbol{x}_{n+1} = \boldsymbol{x}_n + \Delta t \boldsymbol{v}_{n+1}$. For notational convenience, a factor Δt has been absorbed in the multipliers such that the constraint force reads $\boldsymbol{G}^T\boldsymbol{\lambda}/\Delta t$. The upper and lower limits, u and l, in Eq. (A.1), follow from the contact law, and from any joint and motor limits. Since the limits depend on the solution, this is a partially nonlinear complementarity problem. The temporary slack variables, w_l and w_u, are used only internally by the MCP solver. In the present paper the full MCP is solved with a hybrid direct-iterative split solver using the simulation engine AGX Dynamics [40]. The articulated machine and the contact normal forces between the machine and particles are thus solved using a sparse direct block-pivot LDLT solver [41]. The particle contact network and the friction forces between the machine and the particles are solved to lower precision using a projected Gauss-Seidel (PGS) solver [19]. To accelerate the PGS solver computations, parallel processing using spatial domain decomposition and warmstarting [42] is employed.

Expressions for the constraint functions and Jacobians can be found in [19]. These depend on the particle positions and are evaluated at every time-step, based on the present configuration of joints and contacts, computed by means of geometric collision detection.

The regularization and constraint stabilization terms are related to compliance and damping coefficients as follows

$$
\begin{aligned}
\boldsymbol{\Sigma}_{\mathrm{n}} &= \frac{4}{\Delta t^2}\frac{\varepsilon_{\mathrm{n}}}{1 + 4\frac{\tau_{\mathrm{n}}}{\Delta t}}\mathbf{1}_{N_c \times N_c}, \\
\boldsymbol{\Sigma}_{\mathrm{t}} &= \frac{\gamma_{\mathrm{t}}}{\Delta t}\mathbf{1}_{2N_c \times 2N_c}, \\
\boldsymbol{\Sigma}_{\mathrm{r}} &= \frac{\gamma_{\mathrm{r}}}{\Delta t}\mathbf{1}_{3N_c \times 3N_c}, \\
\boldsymbol{\Upsilon}_{\mathrm{n}} &= \frac{1}{1 + 4\frac{\tau_{\mathrm{n}}}{\Delta t}}\mathbf{1}_{N_c \times N_c},
\end{aligned}
\tag{A.4}
$$

where $\varepsilon_{\mathrm{n}} = e_{\mathrm{H}}/k_{\mathrm{n}}$, $\gamma_{\mathrm{n}}^{-1} = k_{\mathrm{n}}c/e_{\mathrm{H}}^2$ and $\tau_{\mathrm{n}} = \max(n_{\mathrm{s}}\Delta t, \varepsilon_{\mathrm{n}}/\gamma_{\mathrm{n}})$, with elastic stiffness coefficient k_{n} and viscosity c. For the Hertz-Mindlin contact law, $e_{\mathrm{H}} = 5/4$, $k_{\mathrm{n}} = e_{\mathrm{H}}E^*\sqrt{d^*}/3$ where $d^* = (d_a^{-1} + d_b^{-1})^{-1}$ is the effective diamater, $E^* = [(1 - \nu_a^2)/E_a + (1 - \nu_b^2)/E_b]^{-1}$ the effective Young's modulus, and ν_a and

ν_b are the Poisson ratios for two contacting particles, a and b. For small relative contact velocities the normal force approximates $\boldsymbol{G}_{\mathrm{n}}^{(n)\mathrm{T}}\boldsymbol{\lambda}_{\mathrm{n}}^{(n)}/\Delta t \approx \varepsilon_{\mathrm{n}}^{-1}\boldsymbol{G}_{\mathrm{n}}^{(n)\mathrm{T}}\boldsymbol{g}_{\mathrm{n}}^{(n)} = \pm k_{\mathrm{n}}\left[\rho^{2e_{\mathrm{H}}-1} + c\rho^{2(e_{\mathrm{H}}-1)}\dot{\rho}\right]\boldsymbol{n}$, which is precisely the Hertz-Mindlin law in Eq. (8).

Collisions are separated into resting contacts and impacts using an impact threshold velocity v_{imp}. If the relative contact velocity is smaller than this value the contacts are modelled as described above. In case of impacts we apply the Newton impact law, $\boldsymbol{G}_{\mathrm{n}}\boldsymbol{v}^{+} = -e\boldsymbol{G}_{\mathrm{n}}\boldsymbol{v}^{-}$ with restitution coefficient e, while preserving all other constraints in the system on the velocity level, $\boldsymbol{G}\boldsymbol{v}^{+} = 0$. This is carried out in an impact stage solve, prior to the main solve for the constrained equations of motions (1)-(3). With this division, the restitution coefficient become the key parameter for modelling the dissipative part of the normal force. For the resting contacts we can simply enforce numerical stability using $\tau_{\mathrm{n}} = 4.5\Delta t$ with little consequence of the artificial damping [43]. In the limit of small time-steps, the physical viscous damping may be used by setting $\tau_{\mathrm{n}} = 5c_{\mathrm{d}}/4$ and not applying Newton's impact law.

Choosing time-step and solver iterations

For a given error tolerance ϵ in a NDEM simulation, the time-step should be chosen [44]

$$\Delta t \lesssim \min(\epsilon d/v_{\mathrm{n}}, \sqrt{2\epsilon d/\dot{v}_{\mathrm{n}}}) \tag{A.5}$$

where v_{n} is the normal contact velocity and $\dot{v}_{\mathrm{n}}$ is the largest potential acceleration that can occur from the forces acting on a particle. In a dense packing the potential acceleration can be estimated by $\dot{v}_{\mathrm{n}} \sim \sigma A_{\mathrm{p}}/m_{\mathrm{p}}$, with particle cross-section $A_{\mathrm{p}} = \pi d^2/4$, mass m_{p} and the characteristic stress σ that may be estimated from known external loads. In the absence of external loads, the potential acceleration coincides with the gravity acceleration.

The number of projected Gauss-Seidel iterations has been found to satisfy the following relation [44]

$$N_{\mathrm{it}} \gtrsim 0.1n/\epsilon \tag{A.6}$$

where n is the length of the contact network (number of particles) in the direction of the dominant stress.

Two examples are considered next. Assume an error tolerance of $\epsilon = 0.01$ and consider a quasi-static system ($v_{\mathrm{n}} \approx 0$) with smallest particle diameter $d_{\mathrm{p}} = 0.01$ m, mass $m_{\mathrm{p}} = 0.001$ kg confined in a cubic container with side length $L = 1.0$ m and wall pressure σ. For a pressure of $\sigma = 1.0$ kPa the acceleration become $a = 78$ m/s^2 and the time-step limits $\Delta t \lesssim 1$ ms. For the larger pressure $\sigma = 100$ kPa we get $a = 7800$ m/s^2 and $\Delta t \lesssim 0.1$ ms. Since the side-length is $n \sim 100$ particle diameters, the number of iterations become $N_{\mathrm{it}} \gtrsim 1000$.

Appendix B. Particle scaling

The use of large pseudo-particles instead of true particle sizes is necessary for manageable number of particles and computational time. With a scale invariant numerical model, the particle sizes can be modified without affecting the bulk properties and without the need to identify a new set of simulation parameters.

We verified scale invariance through the same approach as Obermayr et al. [45]. All geometric quantities were scaled by a factor $\alpha = 0.5$, i.e. particle diameter and relative positions, as well as container and cone penetrometer dimensions. The penetration and compression rates were kept the same, preserving the inertial number. All model parameters are invariant by construction.

For an arbitrarily chosen numerical soil, we compared the original (same geometric quantities as in Section 3) with the scaled models, as presented in Figure B.1 for the triaxial tests. Similarly, Figure B.2 shows the same comparison for the cone penetrometer test. Since the maximum penetration depth, h_{max}, differed between models, we defined the normalized quantity h/h_{max}, where h is the penetration depth. It was observed that the measured stresses were independent of particle size, up to a few percent. The penetration resistances differed only with what was considered noise due to few cone-particle contacts.

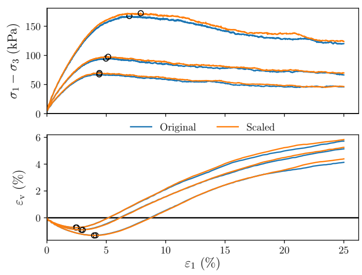

Figure B.1: Deviator stress and volumetric strain versus axial strain for simulated triaxial tests of the original and scaled models. The three confinement pressures are the standard 30, 50 and 100 kPa.

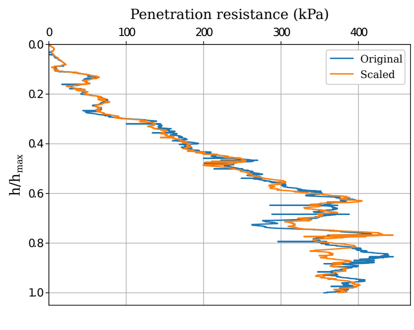

Figure B.2: Penetration resistance versus normalized penetration depth for simulated cone penetrometer tests of the original and scaled models.

References

References

[1] W. Smith, D. Melanz, C. Senatore, K. Iagnemma, H. Peng, Comparison of discrete element method and traditional model-

ing methods for steady-state wheel-terrain interaction of small vehicles, Journal of Terramechanics 56 (2014) 61 – 75.

[2] A. Recuero, R. Serban, B. Peterson, H. Sugiyama, P. Jayakumar, D. Negrut, A high-fidelity approach for vehicle mobility simulation: Nonlinear finite element tires operating on granular material, Journal of Terramechanics 72 (2017) 39–54.

[3] J. De Pue, M. Lamandé, P. Schjønning, W. M. Cornelis, Dem simulation of stress transmission under agricultural traffic part 3: Evaluation with field experiment, Soil and Tillage Research 200 (2020) 104606.

[4] S. Miyai, M. Kobayakawa, T. Tsuji, T. Tanaka, Influence of particle size on vertical plate penetration into dense cohesionless granular materials (large-scale dem simulation using real particle size), Granular Matter 21 (2019) 105.

[5] K. Vennik, P. Kukk, K. Krebstein, E. Reintam, T. Keller, Measurements and simulations of rut depth due to single and multiple passes of a military vehicle on different soil types, Soil and Tillage Research 186 (2019) 120–127.

[6] C. Coetzee, Review: Calibration of the discrete element method, Powder Technology 310 (2017) 104–142.

[7] N. Belheine, Numerical simulation of drained triaxial test using 3d discrete element modeling, Computers and Geotechnics 36 (2009) 320–331.

[8] M. Obermayr, et al., A discrete element model and its experimental validation for the prediction of draft forces in cohesive soil., Journal of Terramechanics 53 (2014) 93–104.

[9] K. Kotrocz, A. M. Mouazen, G. Kerényi, Numerical simulation of soil–cone penetrometer interaction using discrete element method, Computers and Electronics in Agriculture 125 (2016) 63–73.

[10] M. Saarilahti, Soil interaction model. Project deliverable D2 (Work package no. 1) of the Development of a protocol for ecoefficient wood harvesting on sensitive sites (ecowood). EU 5th framework project (Quality of life and management of living resources), Contract No. QLK5-1999-00991 (1999–2002) (2002).

[11] A. T. Abebe, T. Tanaka, M. Yamazaki, Soil compaction by multiple passes of a rigid wheel relevant for optimization of traffic, Journal of Terramechanics 26 (1989) 139–148.

[12] A. Pirnazarov, M. Wijekoon, U. Sellgren, B. Löfgren, K. Andersson, Modeling of the bearing capacity of nordic forest soil, in: Proceedings of the 12th European Regional Conference of the International Society for Terrain-Vehicle Systems, Pretoria, South Africa, 2012, pp. 24–27.

[13] K. Vennik, T. Keller, P. Kukk, K. Krebstein, E. Reintam, Soil rut depth prediction based on soil strength measurements on typical estonian soils, Biosystems Engineering 163 (2017) 78–86.

[14] L. Eliasson, Effects of forwarder tyre pressure on rut formation and soil compaction, Journal of Silva Fennica 39 (2005) 549–557.

[15] K. Nishiyama, H. Nakashima, T. Yoshida, T. Ono, H. Shimizu, J. Miyasaka, K. Ohdoi, 2d fe–dem analysis of tractive performance of an elastic wheel for planetary rovers, Journal of Terramechanics 64 (2016) 23–35.

[16] J. B. Johnson, A. V. Kulchitsky, P. Duvoy, K. Iagnemma, C. Senatore, R. E. Arvidson, J. Moore, Discrete element method simulations of mars exploration rover wheel performance, Journal of Terramechanics 62 (2015) 31–40.

[17] J. De Pue, W. M. Cornelis, Dem simulation of stress transmission under agricultural traffic part 1: Comparison with continuum model and parametric study, Soil and Tillage Research 195 (2019) 104408.

[18] C. Lacoursière, Regularized, stabilized, variational methods for multibodies, in: D. F. Peter Bunus, C. Führer (Eds.), The 48th Scandinavian Conference on Simulation and Modeling (SIMS 2007), 30-31 October, 2007, Göteborg (Särö), Sweden, Linköping University Electronic Press, 2007, pp. 40–48.

[19] M. Servin, D. Wang, C. Lacoursière, K. Bodin, Examining the smooth and nonsmooth discrete element approach to granular matter, Int. J. Numer. Meth. Engng. 97 (2014) 878–902.

[20] V. Acary, B. Brogliato, Numerical Methods for Nonsmooth Dynamical Systems: Applications in Mechanics and Electronics, Springer Verlag, 2008. URL: http://hal.inria.fr/inria-00423530.

[21] F. Radjai, F. Dubois, Discrete-element modeling of granular materials, Wiley-Iste, 2011.

[22] K. G. Murty, Linear Complementarity, Linear and Nonlinear Programming, Helderman-Verlag, Heidelberg, 1988.

[23] K. L. Johnson, Contact mechanics, Cambridge University Press, 1985.

[24] N. Estrada, E. Azéma, F. Radjai, A. Taboada, Identification of rolling resistance as a shape parameter in sheared granular media, Phys. Rev. E 84 (2011) 011306.

[25] J. Y. Wong, Terramechanics and Off-Road Vehicle Engineering, 2nd ed., John Wiley & Sons, 2009.

[26] A. E. FEB99, Procedures for using and reporting data obtained with the soil cone penetrometer, 2003.

[27] A. C. D.-. on Soil, Rock, Standard test method for consolidated undrained triaxial compression test for cohesive soils, ASTM International, 2011.

[28] J. L. Perez, C. Kwok, C. O'Sullivan, X. Huang, K. Hanley, Assessing the quasi-static conditions for shearing in granular media within the critical state soil mechanics framework, Soils and Foundations 56 (2016) 152 – 159.

[29] J. Butlanska, M. Arroyo, A. Gens, Size effects on a virtual calibration chamber, Numerical Methods in Geotechnical Engineering: NUMGE (2010) 225–230.

[30] J. Butlanska, M. Arroyo, A. Gens, Virtual calibration chamber cpt on ticino sand, in: 2nd International Symposium on Cone Penetration Testing, Huntington Beach, CA, USA, 2010.

[31] N. Estrada, A. Taboada, F. Radjaï, Shear strength and force transmission in granular media with rolling resistance, Phys. Rev. E 78 (2008) 021301.

[32] Z. Syed, M. Tekeste, D. White, A coupled sliding and rolling friction model for dem calibration, Journal of Terramechanics 72 (2017) 9–20.

[33] P. Owende, J. Lyons, R. Haarlaa, A. Peltola, R. Spinelli, J. Molano, S. Ward, Operations protocol for eco-efficient wood harvesting on sensitive sites, Ecowood, 2002.

[34] R. Wismer, H. Luth, Off-road traction prediction for wheeled vehicles, Transactions of the ASAE 17 (1974) 8–0010.

[35] T. Anttila, Metsämaan raiteistumisen ennustaminen WES-menetelmää käyttäen. Publications 17. 53 p, Technical Report, University of Helsinki, Department of forest resource management, 1998.

[36] M. Saarilahti, Evaluation of the wes-method in assessing the trafficability of terrain and the mobility of forest tractors–part 2: Comparison of the different wes-models. soil interaction model, Soil interaction model, Appendix Report 3 (2002) 1–28.

[37] D. Potyondy, P. Cundall, A bonded-particle model for rock, International Journal of Rock Mechanics and Mining Sciences 41 (2004) 1329 – 1364. Rock Mechanics Results from the Underground Research Laboratory, Canada.

[38] S. C. Thakur, J. P. Morrissey, J. Sun, J. F. Chen, J. Y. Ooi, Micromechanical analysis of cohesive granular materials using the discrete element method with an adhesive elasto-plastic contact model, Granular Matter 16 (2014) 383–400.

[39] C. Lacoursiére, Regularized, stabilized, variational methods for multibodies, The 48th Scandinavian conference on simulation and modeling (SIMS 2007), Göteborg, 30–31 (2007) 40–48.

[40] Algoryx Simulations, AGX dynamics, 2019. URL: https://www.algoryx.se/products/agx-dynamics/.

[41] C. Lacoursiére, M. Linde, O. Sabelström, Direct sparse factorization of blocked saddle point matrices, Para 2010: State of the Art in Scientific and Parallel Computing, Reykjavik, June 6-9 (2010).

[42] D. Wang, et al., Warm starting the projected gauss-seidel algorithm for granular matter simulation., Computational Particle Mechanics. 3 (2016) 43–52.

[43] D. Wang, M. Servin, T. Berglund, K.-O. Mickelsson, S. Rönnbäck, Parametrization and validation of a nonsmooth discrete element method for simulating flows of iron ore green

pellets, Powder Technology 283 (2015) 475 – 487.

[44] M. Servin, D. Wang, C. Lacoursière, K. Bodin, Examining the smooth and nonsmooth discrete element approaches to granular matter, Journal for Numerical Methods in Engineering 97 (2014) 878–902.

[45] M. Obermayr, C. Vrettos, P. Eberhard, A discrete element model for cohesive soil, in: Proceedings of the international conference on particle-based methods–particles, 2013.